12th International Symposium on Turbulence and Shear Flow Phenomena (TSFP-12)
Osaka, Japan, July 19–22, 2022

# DIRECT NUMERICAL SIMULATIONS OF HYPORHEIC EXCHANGE INDUCED BY ROUGH BEDFORMS

**Guangchen Shen**
Department of Mechanical Engineering
Michigan State University
428 S. Shaw Ln., East Lansing, MI, 48824
shenguan@msu.edu

**Junlin Yuan**
Department of Mechanical Engineering
Michigan State University
428 S. Shaw Ln., East Lansing, MI, 48824
junlin@egr.msu.edu

**Mantha S. Phanikumar**
Department of Civil and Environmental Engineering
Michigan State University
428 S. Shaw Ln., East Lansing, MI, 48824
phani@egr.msu.edu

## ABSTRACT

To understand how different bed morphological scales affect stream hyporheic exchange, pore-resolved direct numerical simulations (DNS) of half channels at a $Re_\tau$ of 1580 on a porous symmetric dune with two different grain-scale roughnesses are conducted. The permeability Reynolds number is $Re_K = 2.5$, representative of streamflows over sandy beds. We show that the dune-shaped bedform leads to large-scale variations of the interfacial pressure, while roughness superimposed on the bedform modifies the pressure variation, as well as the wall friction and shear penetration depth. Characteristics of the subsurface flow are more sensitive to the roughness texture when a bedform is present than when it is not. The results highlight the importance of nonlinear interactions between the effects of roughness and those due to bed morphological features at larger scales. DNS such as the ones reported herein can be used to directly characterize the pore-scale dynamics and to gain insights that could improve pore-unresolved models of hyporheic mixing and biogeochemical processes.

## INTRODUCTION

The hyporheic zone, the region in and around a stream channel where groundwater and stream water mix, plays an important role in biogeochemical processes in stream ecosystems (Boano *et al.*, 2014). Streamflows can be idealized as turbulent open channel flows bounded by permeable beds made of packed sediment grains on the sides and the bottom. In natural streamflows, the bed surface morphologies are multiscale and often self-affine fractals, consisting of large-scale bedforms (e.g. ripples and dunes that are orders of magnitude larger than individual grains) and smaller-scale features, down to the bed roughness at the scale of a grain.

Bedforms can induce significant form resistance, production of turbulence and surface transport. Most analyses and models on the role of bed morphology on the surface-subsurface exchange focused on the scale of the bedforms. Knowledge on the effect of small-scale bed features down to the grain roughness is very limited. The bed roughness has been either ignored or modeled heuristically based on the same approach as for impermeable walls. From the literature of impermeable-wall turbulence , wall roughness is known to enhance the momentum transfer toward the wall and dynamically modify the near-wall flow (Jiménez, 2004). The effects become more important in non-equilibrium flows (Yuan & Piomelli, 2015; Mangavelli *et al.*, 2021) subject to strongly varying longitudinal pressure gradients in space and time, which can be induced by the presence of bedforms.

Some insights into how small-scale features of bed topography may play a role in the exchange were provided by a few studies on multiscale or fractal bed topographies (Aubeneau *et al.*, 2015; Lee *et al.*, 2020). They showed that the interfacial flux and bed storage (i.e., retention of surface flow in the bed) increase with small-scale bed features. Our earlier work (Shen *et al.*, 2020, 2022) based on pore-resolved DNS revealed that, on a macroscopically flat bed (without bedform), grain-scale roughness yields significant volumetric flux into the sediment. It also induces significant subsurface flow and storage as a result of multiscale pressure variations at the sediment-water interface (SWI), a mechanism termed "advective pumping" by interfacial pressure, first observed for bedforms (Elliott & Brooks, 1997*b*). Given the multiscale nature of a realistic stream bed, however, it is not clear whether the roughness effects described above are still significant in the presence of a bedform.

The objective of this work is to identify to what extent the grain-scale bed roughness affects the exchange of water between the surface and subsurface flows induced by a dune-shape bedform. To this end, pore-resolved DNS simulations of turbulent half-channel flows bounded by a dune-shaped permeable bed with two different bed roughnesses are carried out and compared.

## PROBLEM FORMULATION

### Governing Equations

We solve the equations of conservation of mass and momentum governing the incompressible flow of a Newtonian

Table 1. Summary of parameters. $D$ is the grain diameter; $L_{x_i}$ is the simulation domain size in $x_i$; $Re_K = 2.5$, $Re_\tau = 1580$, $D^+ = 79$. $\Delta x^+$, $\Delta y^+$, and $\Delta z^+$ are DNS grid sizes in $x$, $y$ and $z$, respectively, normalized using the viscous length scale $\nu/u_\tau$.

| | Roughness | $D/\delta$ | $H_s/\delta$ | $H/\delta$ | $\lambda/\delta$ | $L_c/\lambda$ | $(L_x, L_z)/\delta$ | $(\Delta x^+, \Delta y^+_{\min}, \Delta z^+)$ |
|---|---|---|---|---|---|---|---|---|
| Case 1 | Regular | 0.05 | 2 | 0.15 | 3 | 0.5 | $(3, 1)$ | $(3.7, 0.3, 4.1)$ |
| Case 2 | Random | 0.05 | 2 | 0.15 | 3 | 0.5 | $(3, 1)$ | $(3.7, 0.3, 4.1)$ |

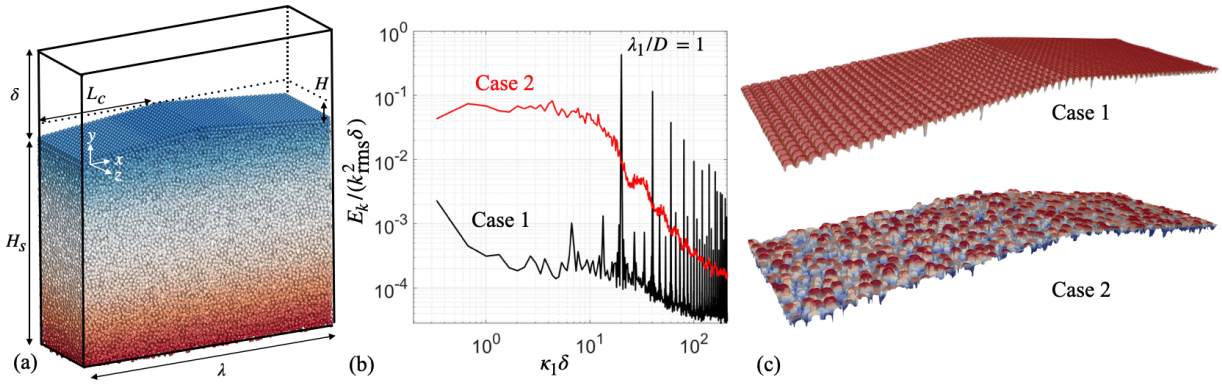


Figure 1. (a) Simulation domain and synthesized bedforms with either regular (Case 1) or random (Case 2) bed roughnesses shown in (c) colored by $y$. (b) Streamwise power spectral density of local roughness height fluctuations.

fluid:

$$\frac{\partial u_i}{\partial x_i} = 0, \tag{1}$$

$$\frac{\partial u_j}{\partial t} + \frac{\partial u_i u_j}{\partial x_i} = -\frac{\partial P}{\partial x_j} + \nu\nabla^2 u_j + F_j. \tag{2}$$

Here, $x_1$, $x_2$ and $x_3$ (or $x$, $y$ and $z$) are, respectively, the streamwise, vertical and spanwise directions, and $u_j$ (or $u$, $v$ and $w$) are the velocity components in those directions; $P = p/\rho$ is the modified pressure, where $p$ is the static pressure and $\rho$ the density. The term $F_j$ is a body force imposed by an immersed boundary method (Yuan & Piomelli, 2014) to impose no-slip boundary conditions on the fluid-solid interface in a Cartesian grid. Details of the Navier-Stokes simulations were described by Shen *et al.* (2020). Symmetric boundary conditions are applied at both top and bottom boundaries of the simulation domain. Periodic conditions are applied at $x$ and $z$ boundaries. A constant mean pressure gradient is used to drive the flow. A double-averaging (DA) decomposition of an instantaneous flow variable $\phi$ to differentiate the turbulent fluctuation ($\phi'$) from the spatial fluctuation of the time-mean value ($\widetilde{\phi}$) (Raupach & Shaw, 1982) is applied: $\phi(\vec{x},t) = \langle\overline{\phi}\rangle(x,y) + \widetilde{\phi}(\vec{x}) + \phi'(\vec{x},t)$, where $\overline{\phi}$ is the temporal average and $\langle\phi\rangle$ is the intrinsic line average along $z$.

## Parameters

The simulation domain includes both the surface flow and sub-surface flow regions (Figure 1(a)). The elevation of $y = 0$ is set at the bedform trough elevation. $\delta$ is the half-channel height measured from $y = 0$; $H_s = 2\delta$ is the sediment depth measured downward from $y = 0$ to the bottom boundary of the simulation domain. $H = 0.15\delta$ is the bedform height measured from $y = 0$ to the dune crest. The bedform wavelength is $\lambda = 3\delta$. A symmetric dune is studied, with $L_c = \lambda/2$. The bedform geometry matches that studied by Cardenas & Wilson (2007).

Details of the simulations and parameters are listed in Table 1. Two cases are considered, one with regular roughness (Case 1), in which the arrangement of grains in the uppermost layer is regular, and the other with random arrangements of uppermost-layer grains (Case 2). In both cases, the same porosity of 0.4 is imposed in the bulk of the sediment. The friction Reynolds number and permeability Reynolds number are the same for both cases: $Re_\tau = \delta u_\tau/\nu = 1580$ and $Re_K = \sqrt{K}u_\tau/\nu = 2.5$, where $K$ is the permeability. The grain diameter in wall units is $D^+ = Du_\tau/\nu = 79$. The values of $Re_K$ and porosity match those in experimental measurements with a flat sediment bed by Voermans *et al.* (2017). $D^+$ is the same as the values used in Shen *et al.* (2020, 2022), which matched the values used by Voermans *et al.* (2017) in Case L12 therein. Here, the friction velocity $u_\tau$ is obtained from the streamwise average of the peak magnitudes of the total shear stress profiles (sum of the viscous, Reynolds and dispersive shear stresses): $u_\tau = \left[(1/L_x)\int_o^{L_x}\left(\nu\partial\langle\bar{u}\rangle/\partial y - \langle\overline{u'v'}\rangle - \langle\widetilde{u}\widetilde{v}\rangle\right)dx\right]^{1/2}$, where $L_x$ is the domain size in the $x$-direction. The number of grid points are 1280, 1147 and 384 in $x$, $y$ and $z$, respectively. The grain geometry is resolved by at least 20 grid points in each direction. The $y$ mesh is refined in the region bounded by the trough and the peak of the dune. The total simulation time used for data collection is around 10 large-eddy turn-over times (LETOTs, defined as $\delta/u_\tau$).

| Cases | $x_c/D$ | $y_c/D$ | $\theta$ | $L/D$ | $C_D$ |
|---|---|---|---|---|---|
| Present | 0.72 | 0.26 | 47.4 | 0.71 | 1.32 |
| Mittal (1999) | – | – | 47.2 | 0.72 | 1.26 |
| Taneda (1956) | 0.68 | 0.25 | 48.6 | – | 1.26 |

Table 2. Validation of spatial resolution of grains by comparing various characteristics of a uniform flow past a single sphere at $Re = 75$ with results from DNS of Mittal (1999) and experiments of Taneda (1956).

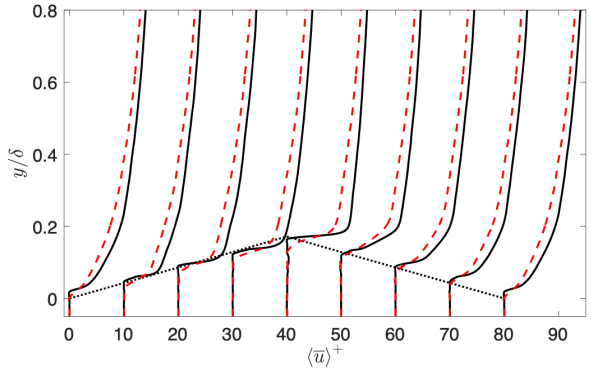


Figure 2. Profiles of time- and spanwise-averaged streamwise velocity: ——— Case 1, - - - Case 2. - - - Local bedform height.

To evaluate the adequacy of the grid size in resolving the pore flow, additional simulations of a single sphere, resolved by 25 grid points in each direction, in a uniform unbounded flow was conducted at a Reynolds number $UD/\nu$ (where $U$ is the uniform freestream velocity and $D$ is the sphere diameter) of 75, comparable to the local Reynolds number at the SWI represented by $D^+ = 79$. The simulation setup is similar to that of Mittal (1999). Results are compared to both those of Mittal (1999) and the experimental measurements of Taneda (1956) in Table 2. The results are 1-6% different for the flow characteristics (separation angle $\theta$, recirculation bubble size $L$ and recirculation center location $(x_c, y_c)$) and 5% for the drag coefficient $C_D$. The comparison gives confidence that the pore flow herein, especially the local mean shear layers and drag force, are overall well captured by the spatial resolution.

The porous bedforms are immobile and modeled as closely packed mono-disperse hard spheres. The locations of the grains are determined based on molecular dynamics simulations (see details in Shen *et al.* (2020)). Two bedforms with the same macroscopic dune geometry but different roughnesses at the uppermost layer are synthesized. One is the "regular" case (Case 1), formed by regular distribution in $(x,z)$ of uppermost-layer grains, and the other is the "random" case (Case 2) formed by random grain distribution of grains in both $(x,z)$ and $y$. Statistically, both roughnesses are similar to those imposed on a flat bed in Shen *et al.* (2020, 2022). Specifically, the random roughness yields a larger Taylor microscale of the roughness height and a larger root-mean-square height (Shen *et al.*, 2020).

Figures 1(c) compare the bed surfaces in Cases 1 and 2, showing the differences in grain arrangement at the top of the bedform. To quantify the differences between the two roughness geometries, the one-dimensional power spectra ($E_k$) of local roughness heights measured from the bedform surfaces are compared in Figures 1(b) as functions of the streamwise wavenumber ($\kappa_1 = 1/\lambda_1$, where $\lambda_1$ is the streamwise wavelength). As expected, similar spectral distributions as those seen on a macroscopically flat bed in Shen *et al.* (2022) are observed here, as the same types of roughness are imposed. Below the bed surface, a random distribution of grains is used in both cases.

## RESULTS

Results for Cases 1 and 2 are compared to understand how different bed roughnesses may affect the SWI turbulence and the subsurface flow in the presence of a bedform.

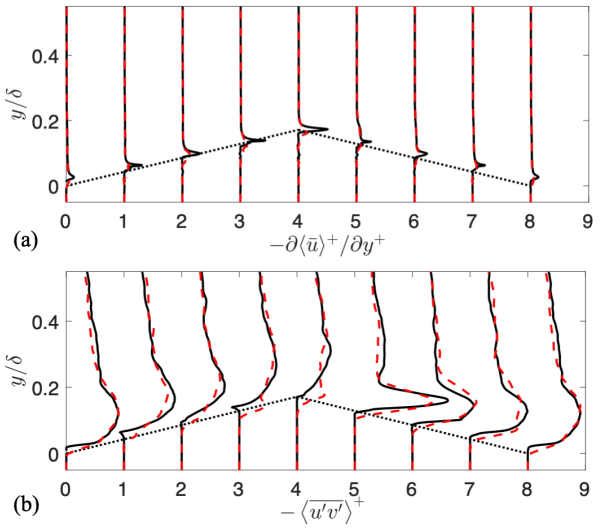


Figure 3. Profiles of (a) viscous and (b) Reynolds shear stresses: ——— Case 1, - - - Case 2. - - - Local bedform height.

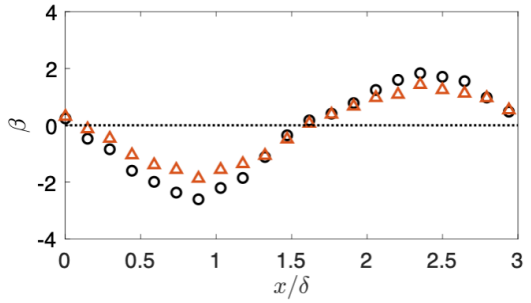


Figure 4. Streamwise variations of of the Clauser parameter: ○ Case 1, △ Case 2.

## Velocity Statistics

The $y$ profiles of the time- and spanwise-averaged streamwise velocity normalized by $u_\tau$ are compared in Figure 2. They show a thinner shear layer on the bed as the flow is accelerated toward the bedform crest, and a thicker shear layer during flow deceleration after the crest. The random roughness leads to a lower bulk velocity in the half channel compared to the regular one and, consequently, results in a 17% higher friction coefficient, $C_f = 2(u_\tau/U_\delta)^2$ (where $U_\delta$ is the mean velocity at the channel centerline), of 0.0109 compared to 0.0093 in the regular-roughness case. The higher $C_f$ is due to the larger effective length scale of the random roughness enhancing the local wall friction on the bedform surface, consistent with the observations made on a macroscopically flat bed by Shen *et al.* (2020).

Profiles of the viscous shear stress normalized by local wall units ($u_\tau$ and viscous length scale $\nu/u_\tau$) are shown in Figure 3(a). Despite the flow deceleration on the lee side and a sharp edge of the bedform at its crest, no mean flow separation (or change of sign of the $y$-gradient of streamwise mean velocity) is observed. This may be because that a permeable wall promotes inner-outer interaction in a turbulent boundary layer and, consequently, reduces the likelihood of pressure-gradient-induced flow separation. The Reynolds shear stress profiles are compared between the two cases in Figure 3(b). They demonstrate deeper penetration of turbulence into the bed on the random roughness than the regular one, indicating dependence of wall-normal mean momentum transfer on the

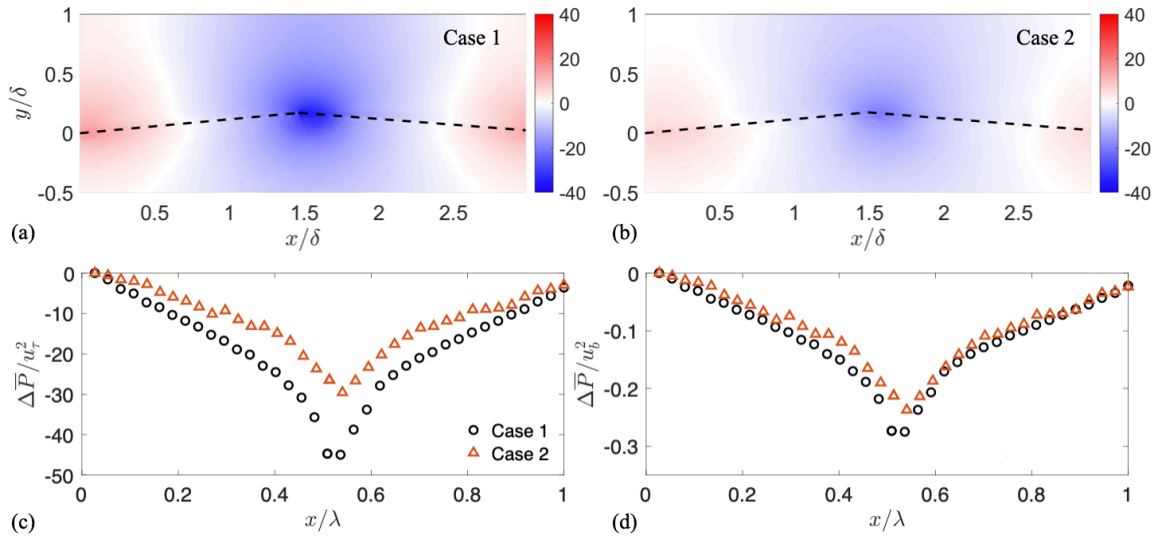


Figure 5. Contours of time- and spanwise-averaged modified pressure ($P$) normalized by $u_\tau^2$, in Case 1 (a) and Case 2 (b). - - - Bedform height. Streamwise distributions of interfacial pressure differences (with respect to the pressure value at dune trough, $x = 0$), normalized based on friction velocity (c) or bulk velocity (d).

roughness details. On the lee side, different from the viscous shear stress which reaches the maximum values on the bed surface, the maximum magnitudes of the Reynolds shear stress are reached consistently at the crest elevation of the dune, probably due to strong TKE production near the dune crest and subsequent convection of new turbulence downstream.

## Pressure Variations

To quantify the strength of half-channel flow acceleration and deceleration due to the bedform, the Clauser parameter $\beta(x) = (\delta^*/|\tau|_{\max})(dp_\delta/dx)$ is calculated and shown in Figure 4. Here, $dp_\delta/dx$ is the streamwise gradient of the static pressure at the channel centerline, $\delta^*(x)$ is the local displacement thickness, and $|\tau|_{\max}(x)$ is the local maximum total shear stress magnitude at an $x$ location. In both cases, $\beta$ takes negative values (indicting favorable pressure gradients, FPG) on the stoss side and positive ones (adverse pressure gradient, APG) on the lee side. The regular roughness (Case 1) yields larger $\beta$ magnitudes in both signs than does the random roughness (Case 2), due to both a stronger centerline pressure gradient (shown later) and a lower wall friction in Case 1. The $\beta$ in the APG region takes values up to around 2, indicating relatively weak pressure gradient induced by the bedform. To investigate the effect of wall permeability on APG flow and separation in the context of hyporheic exchange, one needs to investigate other bedform shapes, such as asymmetric bedforms, that generate stronger pressure gradients.

The distribution of the time- and spanwise-averaged pressure across the half channel and inside the permeable bed is compared in Figure 5 (a,b). As expected, the bedform introduces negative streamwise pressure gradients on the stoss side and positive gradients on the lee side. Similar to what was observed by Cardenas & Wilson (2007) using Reynolds-averaged Navier-Stokes simulations of surface flows only, the minimum pressure is located at the crest of the bedform.

The pressure distribution along the SWI drives the flow in the sediment and controls the surface-subsurface transport. The time-averaged interfacial pressure (measured using $\Delta\overline{P}$ defined as the difference of local interfacial pressure from its value at the dune trough) non-dimensionalized using either the average bulk velocity $u_b$ or $u_\tau$ is shown in Figures 5 (c) and (d). When normalized using $u_\tau^2$ (Figure 5 (c)), the pressure variation induced by the random roughness is significantly weaker (by almost a half in magnitude) than that generated by the regular one. However, the streamwise profiles almost collapse when the pressure drop is normalized using $u_b^2$ instead (Figure 5 (d)).

To explain the approximate scaling of interfacial pressure variation on $u_b^2$, assume that the half-channel flow is steady and inviscid, to which the Bernoulli's equation applies along a streamline (ignoring the hydrostatic pressure). Together with the conservation of mass, one obtains: $\Delta P(x) = P(x) - P_o = (1/2)V_o^2[1 - A_o/A(x)]$, where the subscript "o" denotes the reference point (i.e. $x = 0$), and $V$ and $A$ are the velocity magnitude and the cross-sectional fluid area of the half channel, respectively. It follows that, for a given dune geometry (i.e. a given $A_o/A(x)$ ratio), $\Delta P$ varies as a quadratic function of velocity in the region of approximatley inviscid flow, which can be represented using $u_b$. Notice in Figure 5 (c) that the scaling based on $u_b$ does not collapse perfectly the two cases, as the Bernoulli's equation does not apply exactly. Nevertheless, these observations imply that the difference in pressure variation at the SWI between the two cases is mainly due to the higher wall resistance (as shown by $C_f$) in the random case leading to a reduced mass flux in the surface flow. According to the pumping mechanism (Elliott & Brooks, 1997*b*), a difference in interfacial pressure is expected to change the subsurface flow, which is discussed next.

## Subsurface Particle Transit Times ($\tau$)

The role of hyporheic zones (i.e., subsurface flows) in transforming the chemical signature of stream water depends, among other factors, on the exchange fluxes of water and solutes (nutrients, dissolved organic carbon and oxygen), as well as the transport time scales which are often described using distributions of transit times (Harman, 2015). Here, we focus on the transit time, which is defined as the time spent by a parcel of water in the sediment, after its entry into the sediment and before its exit from the sediment back to the surface flow.

The transit time is calculated based on a particle-tracking method, which has been used with pore-scale simulation data in a few studies (for example, Kim & Kang (2020)). The

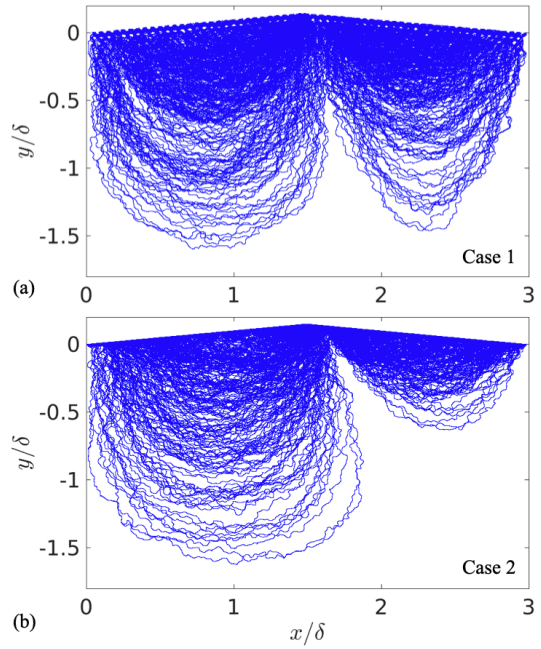


Figure 6. Subsurface flow paths in Cases 1 (a) and 2 (b).

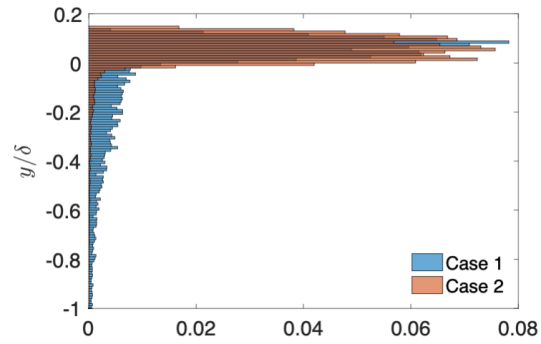


Figure 7. Probability density functions of the maximum depths reached by individual flow paths (quantified using the lowest $y$ values reached).

work of Shen *et al.* (2022) and the present work represent the first attempts in using the particle tracking approach based on turbulent flow DNS. Specifically, a large number of tracked fluid parcels are seeded uniformly on the bedform surface and traced into the bed, yielding a large collection of three-dimensional (3D) subsurface flow paths for each case. The tracking is based on the convection of the 3D time-mean velocity only: $dx_i/dt = \overline{u}_i[x_i(t)]$, where $x_i(t)$ is the parcel location and $t$ is a fictitious time used for the tracking. Once a subsurface flow path is determined, the transit time (denoted by $\tau$) for the corresponding fluid parcel is calculated as the total time it spends along the path. In total, around $o(10^6)$ parcels are released for each case. The advection by instantaneous turbulent fluctuations $u_i'$ is not accounted for. This is because, at the present $Re_K$ of $o(1)$ representative of sandy river beds, the magnitudes of normal Reynolds stress components were shown to be significantly smaller than those of the form-induced stresses in the sediment below the Brinkman layer, which is very thin (20% to 30% of grain diameter) (Shen *et al.*, 2020). At a higher $Re_K$ range, however, the effect of $u_i'$ inside the sediment on the transit times is likely to be more important and the turbulent advection of parcels should not be neglected.

Figure 8 compares the tracked subsurface flow paths. For

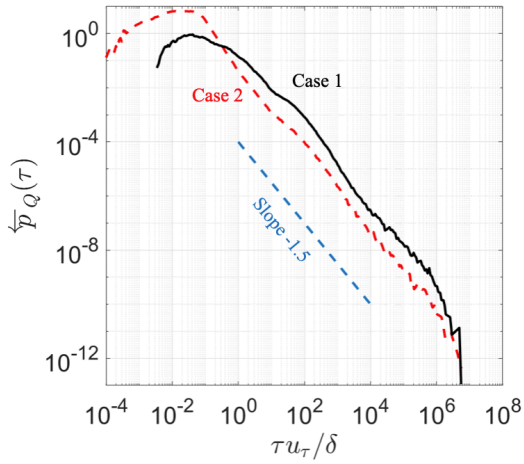


Figure 8. Probability density functions of transit times. - - - Fitted power law with slope indicated.

Table 3. The 50th and 95th percentiles of transit time distributions. All times are normalized by $\delta/u_\tau$.

| | Interface | $\tau_{50}$ | $\tau_{95}$ |
|---|---|---|---|
| Case 1 | Regular | 3 | 385 |
| Case 2 | Random | 0.09 | 7.47 |

both cases, multiscale subsurface flow paths are induced, with the longest ones characterized by roughly a half of the bedform length scale $\lambda$. The general pattern is consistent with observations in existing numerical and experimental data of subsurface flows induced by bedforms (Cardenas & Wilson, 2007; Elliott & Brooks, 1997*a*). Here, the regular roughness is shown to induce a larger fraction of deep-reaching paths and, consequently, overall longer transit times. This is probably due to the higher-magnitude interfacial pressure variation observed in Figure 5 for this case. Figure 7 shows the probability density function (PDF) of the maximum depths (measured using the minimum $y$ value along a flow path) reached by the subsurface paths; the integral area equals one. It is evident that a larger fraction of the paths in the regular case reaches beneath the trough of the bedform (i.e., $y = 0$) than in the random case.

The backward transit-time distributions, $\overleftarrow{p}_Q(\tau)$, defined as the PDF of parcel travel times in the bed (Harman, 2015) are calculated based on the tracked paths for each case and compared in Figure 8. The transit time values are normalized using $\delta/u_\tau$. The distributions in both cases display power-law decays with a slope of around $-1.5$ at large transit times. The existence of a heavy tail of this kind is consistent with experimental observations by Aubeneau *et al.* (2015) and results of numerical simulations obtained by Lee *et al.* (2020) of exchanges induced by multiscale bed geometries, and also indicates that the sediment domain in the DNS simulations is sufficiently large (in both $x$ and $y$) to capture deeper flow paths. Compared to our earlier flat-bed results (Shen *et al.*, 2020) which showed a power-law slope of around $-1.3$, the inclusion of a bedform does not appear to significantly modify the probability of paths with very long transit times. However, the addition of a bedform leads to a difference between the two cases that is opposite from the flat-bed results: the regular roughness produces higher probabilities of flow paths with very long transit times compared to the random one, while results without the bedform Shen *et al.* (2020) showed that the

random roughness yields more long-transit-time paths instead.

The differences in transit time distributions between the two cases are quantified in Table 3, using the 50th and 95th percentiles (denoted as $\tau_{50}$ and $\tau_{95}$, respectively) of the transit-time distributions. Here, $\tau_{50}$ represents the central tendency of the distribution, while $\tau_{95}$ is considered as a characteristic time associated with the rare, long-transit-time paths. The comparison shows that both indicators in the regular case are two orders of magnitude higher than in the random case. An important conclusion that follows is that the difference in grain-scale roughness texture on top of a bedform affects the flow deep in the sediment and significantly modifies the transit time distributions.

## CONCLUSIONS

Pore-resolved DNS simulations of half-channel flows bounded by immobile permeable dune-shaped walls are carried out at $Re_K = 2.5$ and $Re_\tau = 1580$, to characterize the effects of two bed roughnesses, regular and random, on the interfacial and subsurface flows. The mean velocity profiles show that the roughness modifies the flow velocity near the SWI, resulting in a difference in the friction coefficient depending on the roughness texture. The random roughness yields a higher friction coefficient and deeper shear penetration than the regular roughness, consistent with observations made in the absence of the bedform (Shen *et al.*, 2022).

The presence of bedform is shown to induce static pressure variations along the bedform surface due to the acceleration and the subsequent deceleration of the half-channel flow, consistent with observations from a large body of work on permeable and impermeable bedforms. Surprisingly, the roughness textures modify significantly the interfacial pressure variation induced by the bedform: a larger pressure variation is observed on the bedform with regular roughness than that with the random one. This is contrary to the observations made without the bedform where the random roughness induces more intense pressure variations at the roughness length scales. This difference in hyporheic exchange between the flat-bed and bedform cases is attributed to the different roles played by the roughness: on a macroscopically flat bed, roughness protuberances create roughness-scale pressure heterogeneity, while on a bedform, the roughness leads to higher wall friction, reducing the mass flux through the half channel and consequently the pressure variations.

Correspondingly, contrary to the flat-bed flows where the random roughness augments mass storage in the bed by inducing longer and deeper flow paths and longer transit times, with the presence of bedform the opposite is observed. The results show that grain-scale roughness superimposed on a bedform does not simply act as a smaller-scale "bedform" with a lesser effect on pumping. Instead, roughness modulates the bedform-induced exchange, by changing the macroscopic pressure distribution along SWI. This work demonstrates that grain-scale roughness on top of a bedform should not be ignored when studying hyporheic exchange, as shown by its influence on the pressure variation and transit times.

## REFERENCES

Aubeneau, A. F., Martin, R. L., Bolster, D., Schumer, R., Jerolmack, D. & Packman, A. I. 2015 Fractal patterns in riverbed morphology produce fractal scaling of water storage times. *Geophys. Res. Lett.* **42**, 5309–5315.

Boano, F., Harvey, J. W., Marion, A., Packman, A. I., Revelli, R., Ridolfi, L. & Worman, A. 2014 Hyporheic flow and transport processes: Mechanisms, models, and biogeochemical implications. *Reviews of Geophysics* **52**, 603–679.

Cardenas, M. B. & Wilson, J. L. 2007 Dunes, turbulent eddies, and interfacial exchange with permeable sediments. *Water Resour. Res.* **43**, W08412–1–16.

Elliott, A. H. & Brooks, H. 1997*a* Transfer of nonsorbing solutes to a streambed with bed forms: Laboratory experiments. *Water Resour. Res.* **33**, 137–151.

Elliott, A. L. & Brooks, H. 1997*b* Transfer of nonsorbing solutesto a streambedwith bed forms: Theory. *Water Resour. Res.* **33**, 123–136.

Harman, C. J. 2015 Time-variable transit time distributions and transport: Theory and application to storage-dependent transport of chloride in a watershed. *Water Resour. Res.* **51**, 1–30.

Jiménez, J. 2004 Turbulent flows over rough walls. *Annu. Rev. Fluid Mech.* **36**, 173–196.

Kim, J. S. & Kang, P. K. 2020 Anomalous transport through free-flow-porous media interface: Pore-scale simulation and predictive modeling. *Advances in Water Resources* **135**, 103467.

Lee, A., Aubeneau, A. F. & Cardenas, M. B. 2020 The sensitivity of hyporheic exchange to fractal properties of riverbeds. *Water Resour. Res.* **56**, e2019WR026560–1–15.

Mangavelli, S. C., Yuan, J. & Brereton, G. J. 2021 Effects of surface roughness topography in transient channel flows. *J. Turbul.* **22**, 434–460.

Mittal, R. 1999 A Fourier–Chebyshev spectral collocation method for simulating flow past spheres and spheroids. *International Journal for Numerical Methods in Fluids* **30** (7), 921–937.

Raupach, M. R. & Shaw, R. H. 1982 Averaging procedures for flow within vegetation canopies. *Bound.-Lay. Meteorol.* **22**, 79–90.

Shen, G., Yuan, J. & Phanikumar, M. S. 2020 Direct numerical simulations of turbulence and hyporheic mixing near sediment–water interfaces. *J. Fluid Mech.* **892**, A20.

Shen, G., Yuan, J. & Phanikumar, M. S. 2022 Quantifying the effects of bed roughness on transit time distributions via direct numerical simulations of turbulent hyporheic exchange. *Water Resour. Res.* **58**, e2021WR030503–1—16.

Taneda, S. 1956 Experimental investigation of the wake behind a sphere at low Reynolds numbers. *Journal of the Physical Society of Japan* **11** (10), 1104–1108.

Voermans, J. J., Ghisalberti, M. & Ivey, G. N. 2017 The variation of flow and turbulence across the sediment–water interface. *J. Fluid Mech.* **824**, 413–437.

Yuan, J. & Piomelli, U. 2014 Numerical simulations of sink-flow boundary layers over rough surfaces. *Phys. Fluids* **26** (1), 015113.

Yuan, J. & Piomelli, U. 2015 Numerical simulation of a spatially developing accelerating boundary layer over roughness. *J. Fluid Mech.* **780**, 192–214.